FCC

March 10, 2025

Sensitivity study of the search for the rare decay $D^0 \to \pi^+\pi^-\nu\bar{\nu}$ at FCC-ee

Tabea Hacheney[a], Lars Röhrig[a,b], Dominik Mitzel[a], Angelo Di Canto[c], Stéphane Monteil[b]

[a] *Fakultät Physik, Technische Universität Dortmund, Dortmund, Germany*
[b] *Université Clermont Auvergne, CNRS/IN2P3, LPC, Clermont-Ferrand, France*
[c] *Physics Department, Brookhaven National Laboratory, Upton NY, United States*

Abstract

This note presents a sensitivity study for the rare charm decay $D^0 \to \pi^+\pi^-\nu\bar{\nu}$ at the Future Circular Collider (FCC-ee) operated a the Z pole with 6×10^{12} produced Z bosons. Preliminary results indicate that an observation with a significance $5(3)\sigma$ at the level of 1.6×10^{-6} (9.7×10^{-7}) could be possible, which is within the parameter space allowed in BSM models. The presented results are very preliminary and will be developed further.

Contents

1 Introduction

After the discovery of the Higgs boson at CERN's Large Hadron Collider (LHC) in 2012 [1,2], one of the main goals of current and future experiments is to precisely determine its properties, which, if found to be inconsistent with the Standard-Model (SM), could give indirect hints of new physics appearing at the TeV scale. To accomplish this task, the experimental high-energy physics community is considering the possibility to build a future electron-positron collider, such as the Future Circular Collider (FCC-ee) [3]. However, the potential of FCC-ee goes well beyond the study of the Higgs boson. When operated at collision energies close to the Z pole, it can also serve as a facility for precise measurements in the sector of flavour physics as addressed by several studies focusing on bottom-hadron decays [4–6]. Despite the large samples of approximately 7×10^{11} $Z \to c\bar{c}$ decays expected to be produced at FCC-ee, FCC-ee's potential in the sector of charmed hadrons remains largely unexplored. The field of charm physics plays an important role in the research program of current flavour experiments, such as LHCb [7] and Belle II [8], as probes for beyond-the-SM (BSM) physics. Of particular interest are rare-charm decays into final states with leptons [9]. Contrary to strange and bottom rare processes, where loop-induced transitions occur through the exchange of up-type quarks (u, c, t), down-type quarks (d, s, b) are exchanged in charm transitions. On the one hand, this makes charm transitions very suppressed, requiring large samples of experimental data to be studied, and subject to large theory uncertainties arising from strong-interaction effects at low energies, which cannot be calculated with perturbative methods. On the other hand, it means that rare charm decays offer complementary sensitivity to those performed with kaons and bottom mesons, giving access to orthogonal interaction couplings that cannot be probed otherwise and making them an alternative avenue for BSM searches.

Important tools for BSM searches that are less affected by theory uncertainties in rare charm decays are null tests, i.e., observables that are negligibly small in the SM due to exact or approximate symmetries or parametric suppression. An example is provided by $c \to u\nu\bar{\nu}$ transitions: their SM branching fractions are tiny and well beyond the experimental reach, so any observation at current facilities would clearly indicate BSM physics [10,11]. Example BSM scenarios that can be tested in $c \to u\nu\bar{\nu}$ decays include new scalar or vector bosons, leptoquarks, or light dark-matter particles mimicking the dineutrino signature. These are all theoretically well-motivated extensions of the SM that can address some of its limitations. Moreover, as the size of their branching fractions depends on neutrino flavour, rare charm dineutrino modes also test BSM physics in a model-independent approach: assuming lepton universality or charged lepton flavour conservation, which are exact symmetries in the SM, model-independent upper limits on branching fractions of flavour-summed dineutrino modes can be derived using $SU(2)_L$ symmetry and existing bounds on the less suppressed charged-lepton modes ($c \to u\ell^+\ell^-$ with $\ell = \mu, e$) [12]. With no additional assumptions about charged lepton flavour symmetries, the upper limits typically reach a few $\times 10^{-5}$. The upper limits are approximately four times smaller when assuming charged lepton flavour conservation and almost 10 times smaller in the case of lepton universality [10–12]. Presently, there is no experimental limit on any of the $c \to u\nu\bar{\nu}$ branching fractions, partly because of the experimental challenge of identifying final states with two neutrinos that leave no signature in the experimental apparatus.

This note describes a sensitivity study for the first measurement of the decay $D^0 \to \pi^+\pi^-\nu\bar{\nu}$ at FCC-ee using an assumed sample of 6×10^{12} produced Z bosons and the IDEA detector concept [13,14]. The decay has been chosen as an ideal example of $c \to u\nu\bar{\nu}$ transitions, since it has the experimental advantage of providing a displaced secondary D^0 decay vertex that can be reconstructed from the two oppositely charged pions. Studies of related decay modes and topologies, such as $D^0 \to K^+K^-\nu\bar{\nu}$, $D^+ \to \pi^+\nu\bar{\nu}$ or $\Lambda_c^+ \to p\nu\bar{\nu}$ [10], are left for future studies. We show that the experimental conditions of e^+e^- collisions, the significant boost of the produced charm quarks, and the hermetic detector concept of the IDEA detector [13, 14], enable efficient reconstruction and selection of $D^0 \to \pi^+\pi^-\nu\bar{\nu}$ decays.

The note is structured as follows. First, section 2 outlines the simulated samples of data used in the analysis and the IDEA detector concept. The analysis strategy follows in section 3, which comprises a candidate selection, estimation of expected backgrounds and determination of the expected sensitivity of the measurement. Final concluding remarks are given in section 4.

2 Detector model and simulated data

The event generator PYTHIA8 [15] is used to simulate the e^+e^- collision, as well as the hadronisation of the outgoing quarks. Modelling of the beam size is taken into account according to the latest beam-size parameters (5.96 µm, 23.8 nm, 0.397 mm) in x, y, and z dimensions, respectively [16]. For background studies, inclusive Z-boson decay samples are generated privately with the production parameters of the so-called winter2023 campaign using EvtGen [17] for modeling the decay of unstable particles. In EvtGen, we use the decay table provided by the Belle II collaboration [18]. With respect to the official FCC-ee samples of the winter2023 campaign, which rely exclusively on PYTHIA8, our approach gives a more realistic generation of the physic processes by accounting also for very rare decays of b and c hadrons, which could be relevant for the presented analysis. Signal $D^0 \to \pi^+\pi^-\nu\bar{\nu}$ decays are also generated using EvtGen assuming uniformly distributed final-state particles in the decay phase space. Only decays of one flavour (D^0) are considered to avoid the occurrence of the signal decay in both hemispheres which would bias the event selection. The following number of events have been generated

$$
\begin{aligned}
N(Z \to b\bar{b}) &= 10^8\,, & N(Z \to c\bar{c}) &= 10^8\,,\\
N(Z \to u\bar{u}) &= 10^8\,, & N(Z \to d\bar{d}) &= 10^8\,,\\
N(Z \to s\bar{s}) &= 10^8\,, & N(Z \to \tau^+\tau^-) &= 10^8\,,\\
N(D^0 \to \pi^+\pi^-\nu\bar{\nu}) &\sim 10^6\,.
\end{aligned}
$$

Here, the leptonic $Z \to \tau^+\tau^-$ has been included to account for 3-prong τ decays into hadrons, which have missing momentum in the final state and are topologically similar to signal candidates.

The detector model is based on the IDEA detector concept [13, 14]. It consists of silicon vertex detectors close to the beam pipe, a drift chamber for quasi-continuos tracking of charged particles, a 2 T solenoid, as well as a dual-readout calorimetry and muon chambers. This model is widely used and tested in the community to derive detector requirements for both flavour and Higgs physics, with flavour-physics studies resulting in the most stringent requirements in terms of vertexing, tracking, and calorimetry [6]. For fast simulation, parametric detector responses have been modelled using DELPHES [19], including the full event reconstruction into particle-flow objects. Particle-specific energy and momentum resolutions are applied following Refs. [20, 21]. For charged hadrons, we assume a particle-identification performance provided by the drift chamber as presented in Ref. [22] (Figure 1).

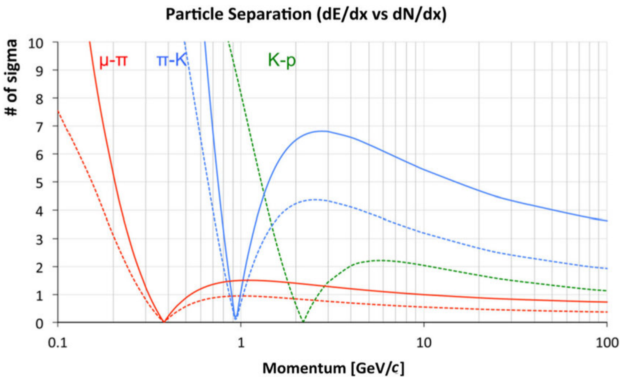

Figure 1: Expected particle-identification performance of the IDEA drift chamber, both for cluster counting (solid lines) and dE/dx measurements (dotted lines), expressed as separation power (in units of Gaussian standard deviations) between different particle species. Reproduced from Ref. [22].

The output, the community-wide `EDM4HEP` [23] standard, has further been processed within the `FCCAnalyses` framework, based on `ROOT`'s `RDataFrame` format [24].

3 Analysis

To estimate the sensitivity of $D^0 \to \pi^+\pi^-\nu\bar{\nu}$ at the FCC-ee, first a candidate reconstruction and selection is developed. In the selection, a cut-based preselection is applied to suppress evident background contributions, followed by the training and evaluation of a two-stage Boosted Decision Tree (BDT). Lastly, the sensitivity is calculated from the estimated efficiencies.

3.1 Candidate reconstruction

The reconstruction starts with the identification of tracks that originate from secondary vertices, well displaced from the primary e^+e^- interaction. The function `get_PrimaryTracks` from the `FCCAnalyses` library [25] identifies "primary" tracks by fitting them to a primary vertex (PV) which is constrained to be in the e^+e^- luminous region (beam spot). The constraint uses the sizes of the luminous region as uncertainties and the origin $(0, 0, 0)$ as reference center. The actual fit, performed by the function `theVertexFit` [26], returns a χ^2 value computed as the sum of the χ_i^2 contribution of each track i, $\chi^2 = \sum_i \chi_i^2$. In an iterative procedure, tracks with a $\chi_i^2 > 25$ are removed from the fitted PV and identified as "secondary" tracks. The position of the PV is then determined and a vertex object is created with the function `VertexFitter_Tk` [25].

Secondary tracks are identified as pions, kaons, or muons using truth-level information. Per-track weights are then assigned to simulate realistic misidentification rates. For pions, a 100% identification probability is assumed by assigning a weight $w = 1$ to all true pions. Momentum-dependent weights emulating kaon-to-pion and muon-to-pion misidentification rates are shown in Figure 2. These are computed as

$$w(p) = 2 \times \int_{\sigma(p)}^{\infty} \mathcal{G}(x)\,\mathrm{d}x, \tag{3.1}$$

where $\mathcal{G}$ is a Gaussian distribution with zero mean and unit width, and $\sigma(p)$ is the assumed momentum-dependent separation between different particle species using cluster counting shown in Figure 1. It is assumed that the particle-identification performance for a given track is independent from the performance of all other tracks. The misidentification of all other particle species is assumed to be negligibly small.

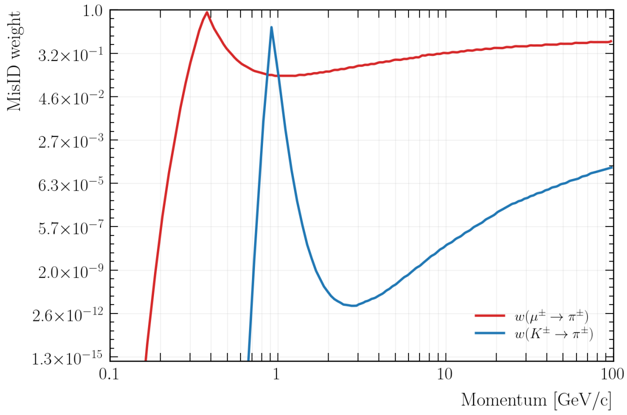

Figure 2: Assumed kaon-to-pion and muon-to-pion misidentification probabilities as a function of momentum.

To reconstruct candidate $\pi^+\pi^-$ secondary vertices from $D^0 \to \pi^+\pi^-\nu\bar{\nu}$ decays, the vertex fitting procedure begins by selecting pairs of oppositely charged pion tracks as seed tracks. Each pair is fit to a common vertex, and the resulting fit must satisfy $\chi^2/\mathrm{ndof} < 7.4$. Candidate $\pi^+\pi^-$ vertices are excluded if, when combined with other charged particles in the event, form good vertices satisfying the same quality requirement. This process continues iteratively until no remaining pion tracks can be used for initial vertex seeding.

Tracks that could not be assigned to any $\pi^+\pi^-$ vertex are subsequently fitted using any combination of two charged tracks as initial vertex seed. Any resulting two-particle vertex consisting of pions, kaons, or muons is considered a D^0 signal candidate. The total misidentification weight w of a candidate is determined as the product of the individual misidentification probabilities of its constituent tracks.

The reconstruction efficiency is defined as the sum of the weights of all reconstructed D^0 candidates over the total number of initial events,

$$\frac{\sum_i w_{i,\mathrm{rec}}}{N_{\mathrm{initial\ events}}} . \tag{3.2}$$

For the signal dataset, this efficiency is found to be 63.4%. The average efficiency for background samples is 54.0%. The subsequent analysis is performed on a candidate-by-candidate basis, treating each candidate as an independent event, even if multiple candidates are reconstructed within the same event.

Non-reconstructed particles such as neutrinos appear as missing energy in the event, which is simply calculated from energy-momentum conservation via

$$\mathrm{ME} = -\sum_{i=0}^{n_{\mathrm{particles}}} \vec{p}_i \,, \tag{3.3}$$

with the index i running over all particle-flow objects and $\vec{p}$ being their respective momentum vector. The presence of two neutrinos in the final state of the signal decay leads to a significant energy imbalance between the signal hemisphere and the opposite hemisphere. To quantify the energy imbalance, as well as other observables of the signal hemisphere, the thrust axis $\vec{t}$ is computed. For this, the `MIGRAD` method of the Minuit minimizer [27] is used to minimize

$$\frac{\sum_i |\vec{p}_i \cdot \hat{t}|}{\sum_i |\vec{p}_i|} = \frac{\sum_i |p_{x_i} \cdot \hat{t}_x + p_{y_i} \cdot \hat{t}_y + p_{z_i} \cdot \hat{t}_z|}{\sum_i \sqrt{p_{x_i}^2 + p_{y_i}^2 + p_{z_i}^2}} \,, \tag{3.4}$$

where the index i denotes each reconstructed particle and $\hat{t}_n$ is the n^{th} component of the thrust vector normalized by the magnitude of $\vec{p}$. This axis is perpendicular to the plane separating the two hemispheres. To make sure it always points towards the signal hemisphere, the thrust axis vector is transformed given the $\pi^+\pi^-$ candidate momentum $\vec{p}_{\pi^+\pi^-}$ via

$$\vec{p}_{\pi^+\pi^-} \cdot \vec{t} \begin{cases} > 0, & \vec{t} \to \vec{t} \\ < 0, & \vec{t} \to -\vec{t} \end{cases} . \tag{3.5}$$

Variable	Requirement
Number of reconstructed π^0 in event	`< 120`
Reconstructed energy of D^0 candidate	`> 1 GeV`
$\mathrm{IP}_{\pi^+\pi^-}$	`< 1 mm`
Total number of reconstructed tracks in event	`< 12`
D^0 candidate is in hemisphere with lowest reconstructed energy	`True`
Missing energy of event	`> 1.2 GeV`
Min. of the IP of the two π from D^0 candidate	`< 1 mm`
Max. of the IP of the two π from D^0 candidate	`< 2 mm`
Flight Distance of D^0 candidate	`< 10 mm`
$\mathrm{IP}_{\pi^+\pi^-} - \mathrm{IP}_{\pi^+\pi^-\mathrm{ME}}$	`> -0.5 mm`
$\mathrm{DIRA}_{\pi^+\pi^-} - \mathrm{DIRA}_{\pi^+\pi^-\mathrm{ME}}$	`> -0.5 rad`
Opening angle α of π's	`< 0.9 rad`
Combined q-jet score of signal and non-signal hemisphere ($q \in [b, u/d, g]$)	`< 1.2`
Combined s-jet score of signal and non-signal hemisphere	`< 1`
c-jet score of signal hemisphere	`> 0.01`
Number of leptons in signal hemisphere	`= 0`
$m(\pi^+\pi^-)$	`< 1.8 GeV`
$m(\pi^+\pi^- ME)$	`< 3 GeV`

Table 1: Requirements used in the preselection of the signal candidates. Signal and background distributions of each variable are shown in Appendix A.

Variables used in the further selection are evaluated relative to the hemisphere containing the signal candidate. This approach captures the key characteristics of the hemisphere associated with the signal decay. The variables showing the highest discrimination power between signal and background are then used to apply a cut-based preselection suppressing the most evident background by about 97.9%. About 61.3% of the signal candidates survive this preselection. The preselection requirements are presented in Table 1. Here, the impact parameter (IP) is defined as the minimum distance of a particle trajectory to the reconstructed PV. The difference of the IP of the D^0 candidate with and without adding information on the missing energy is referred to as $\mathrm{IP}_{\pi^+\pi^-} - \mathrm{IP}_{\pi^+\pi^-\mathrm{ME}}$. The direction angle (DIRA) is the angle between the momentum vector of the signal candidate reconstructed with the two pions $\vec{p}_{\pi^+\pi^-}$ and the vector connecting the PV and the D^0 decay vertex. The response of a neural-network-based jet flavour tagger [28] is used to identify $c\bar{c}$ events. The number of reconstructed π^0 is also used, which is computed by summing the amount of two photon combinations fulfilling certain criteria, such as an opening angle $< \pi$ and an invariant mass in the range $[50, 250]$ MeV. In this approach the same photon can be used to reconstruct multiple π^0 candidates. The difference $m_{\pi^+\pi^-\mathrm{ME}} - m_{\pi^+\pi^-}$ is the difference of the reconstructed invariant mass of the two pion combination and the mass of the D^0 candidate adding the missing energy. Plots showing the signal and background distributions of the variables used in the preselection can be found in Appendix A.

3.2 Selection optimisation

Two BDTs based on an Adaptive Boosting (`AdaBoost`) algorithm [29] are trained to separate signal and background candidates.

The first BDT (BDT1) is trained on the exclusively simulated $D^0 \to \pi^+\pi^-\nu\bar{\nu}$ decays as signal, while the background sample consists of a merged dataset of all inclusive background samples described in section 2. The proportions of the different $Z \to X$ samples reflect the current knowledge: 12.03% $Z \to c\bar{c}$, 15.12% $Z \to b\bar{b}$, 15.84% $Z \to s\bar{s}$, 11.17% $Z \to u\bar{u}$, 15.84% $Z \to d\bar{d}$, and 3.37% $Z \to \tau^+\tau^-$ [30]. The background dataset also includes events with misidentified K and μ tracks with their corresponding misidentification weights.

To validate the training results, the dataset is split into a training set (two-thirds) and a testing set (one-third).

The input variables for BDT1 primarily capture the overall event topology, including hemisphere energy asymmetry, track multiplicity, and the response of the jet flavour tagger. The input variables are selected to ensure minimal correlation within either the signal or background dataset while maximizing their discrimination power. The variables used in the first BDT are:

- c-jet score of signal side,
- combined q-jet score of signal and non-signal side ($q \in [c, b, s, u/d, g]$) (*),
- sum of all combined q-jet scores except c-jet score → likelihood to **not** origin from $Z \to c\bar{c}$ (*),
- number of reconstructed π^0 in event,
- reconstructed energy of D^0 candidate (*),
- total number of charged tracks and total number of particles in event
- total reconstructed energy of charged tracks in event,
- reconstructed energy of charged tracks in the signal hemisphere,
- reconstructed energy of particles in the signal hemisphere,
- reconstructed invariant mass of PV using primary tracks,
- missing energy of event (*),
- number of three-particle vertices and total number of vertices (*),
- total reconstructed energy of event (*),
- energy asymmetry of hemispheres using the reconstructed energy of all particles (*).

Appendix A reports the separation power and importance of each variable, and their linear correlation coefficients. The distribution of the BDT1 response is shown in the left plot of Figure 3. The area under the ROC curve of the classifier (AUC) is 0.844, which displays a successful training.

A minimum threshold on the BDT1 response is chosen by mazimising the figure of merit (FOM) [31]

$$\mathrm{FOM}_{n\sigma} = \frac{\epsilon_{\mathrm{BDT1,sig}}}{\frac{n}{2} + \sqrt{B}}, \tag{3.6}$$

where B is the total expected background yield (as computed in the next section), $\epsilon_{\mathrm{BDT1,sig}}$ is the signal efficiency determined as the ratio of signal yields before ($N_{\mathrm{preselection}}$) and after ($N_{\mathrm{BDT1}}$) the BDT1 requirement $\epsilon_{\mathrm{BDT1,sig}} = \frac{N_{\mathrm{BDT1}}}{N_{\mathrm{preselection}}}$. This metric is particularly useful when the absolute number of signal events is unknown, as it depends on the signal efficiency rather than the total number of signal events. The optimization is performed for $n = 3, 5$, corresponding to $3, 5\sigma$ levels of signal significance. The FOM for either level of significance yields similar BDT1 cut requirements. The evolution of the FOM as a function of the BDT1 cut value for the case $n = 3$ is shown on the left of Figure 4. The optimal BDT1 cut value, at which the FOM reaches its maximum, is found to be > -0.008, which results in a background rejection of 71.8% and a signal efficiency of 76.9%.

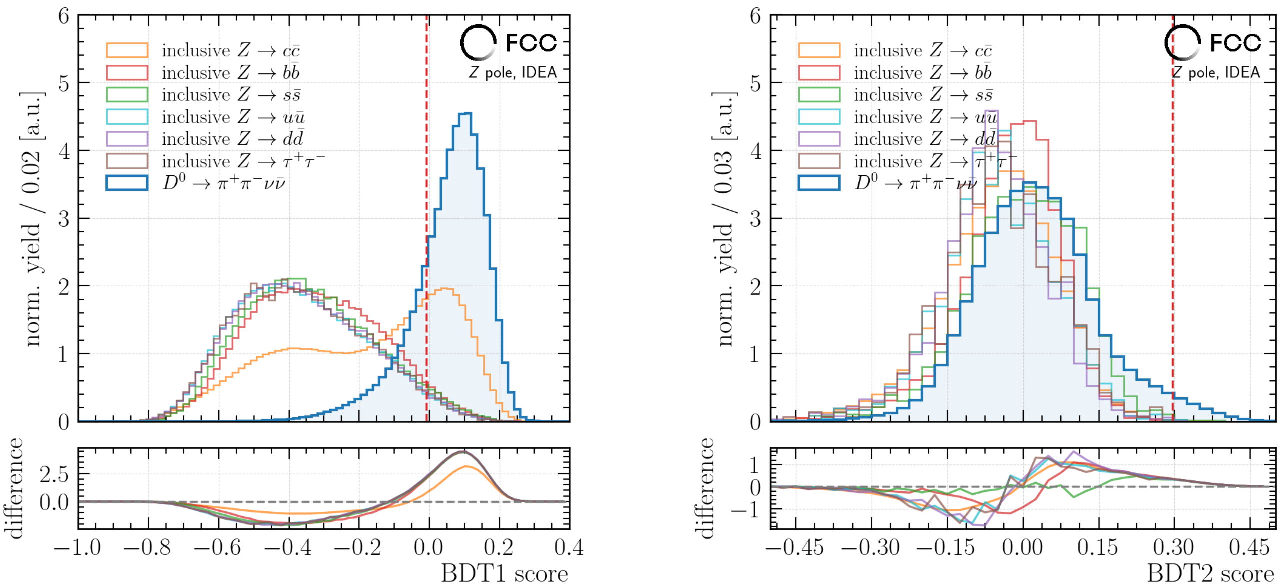

Figure 3: The response of the first BDT (left) and second BDT (right) on all inclusive backgrounds and the signal. The red dotted lines represent the applied BDT cuts.

The second BDT (BDT2) is trained only for events passing the BDT1 requirement and is designed to suppress background events having higher similarities to the signal. It relies on variables that characterize more directly the $D^0 \to \pi^+\pi^-\nu\bar{\nu}$ decays, like the opening angle of the pions or the DIRA. Some BDT1 input variables (marked with an asterisk in the above list) show good separation power even after the BDT1 requirement, as they also catch some important characteristics of the decay itself. Therefore, these variables are again included in the BDT2 training. Additionally, the BDT1 output is itself included as an input variable. The new variables used for training of the BDT2 are:

- BDT1 score,
- $\log(1 - \cos(\theta))$, where θ is the angle between the reconstructed signal-candidate momentum ($p_{\pi^+\pi^-}$) and the thrust axis;
- $\log(1 - \cos(\alpha))$, where α is the angle between the two pion tracks;

- $\log(1 - \angle(\text{fw}, \text{bw}))$, where $\angle(\text{fw}, \text{bw})$ is the angle between the thrust of particles on the signal side and the thrust of particles on the non-signal side;
- distance of closest approach between the two pions (DOCA);
- energy of charged tracks,
- number of tracks and number of π^0 candidates within an angular distance $R = \sqrt{\Delta\phi^2 + \Delta\eta^2} \leq 0.5$ of the reconstructed D^0 momentum ($p_{\pi^+\pi^-}$), with ϕ being the azimuthal angle and η the pseudorapidity.

Appendix A reports the correlation matrix of the BDT2 input variables as well as their separation power and importance. The BDT2 response is shown in the right plot of Figure 3. The AUC for BDT2 is 0.724, which demonstrates a strong classification performance.

The requirement on the BDT2 response is optimized following the same procedure as for BDT1. In this case, the signal efficiency is determined as the ratio of signal yields before (N_{BDT1}) and after (N_{BDT2}) the BDT2 requirement. The optimization computed for the two significance levels yields the same maximum FOM value. The evolution of the FOM as a function of the BDT2 requirement for the $n = 3$ case is shown in the right plot of Figure 4. The BDT2 requirement that maximises the FOM, > 0.292, results in a background rejection of 99.9% and a signal efficiency of 3.8%.

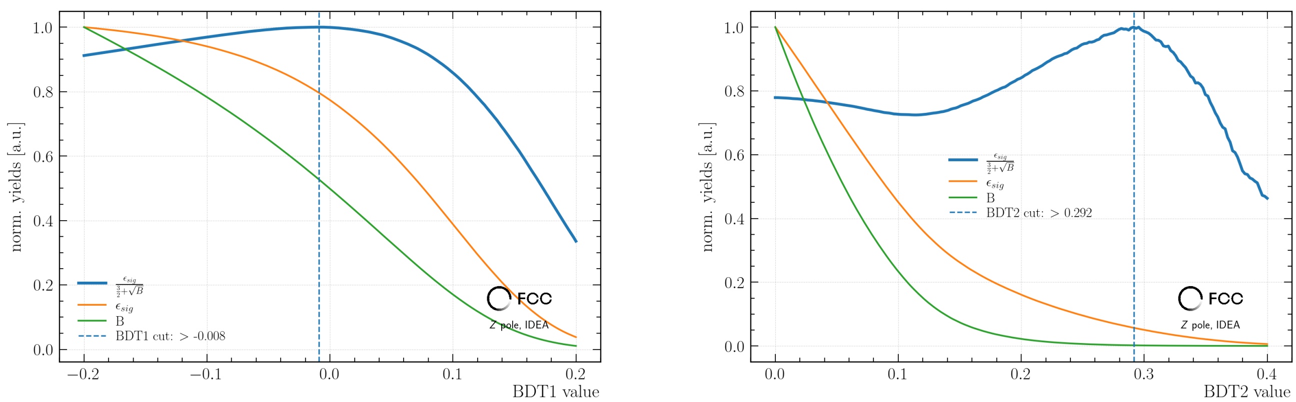

Figure 4: The optimization of the BDT1 (left) and BDT2 (right) cut value is shown by plotting the signal efficiency (ϵ_{sig}, orange), the normalized background yield (B, green), and the FOM$_{3\sigma}$ (blue).

3.3 Sensitivity estimation

To evaluate the sensitivity, the statistical significance of the signal is approximated as

$$s = \frac{S}{\sqrt{S+B}}. \tag{3.7}$$

where S and B are the expected signal and background yields, respectively. The expected number of signal events S is computed from the assumed signal branching fraction $\mathcal{B}(D^0 \to \pi^+\pi^-\nu\bar{\nu})$ as

$$S = 2 \times N_Z \times \mathcal{B}(Z \to c\bar{c}) \times 0.59 \times \mathcal{B}(D^0 \to \pi^+\pi^-\nu\bar{\nu}) \times \epsilon_{\text{total,sig}}, \tag{3.8}$$

where:

- The factor of 2 accounts for the production of both charm and anti-charm quarks per Z decay,
- $N_Z = 6 \times 10^{12}$ is the expected number of produced Z bosons,
- $\mathcal{B}(Z \to c\bar{c}) = 12.03\%$ is the branching fraction of the Z to a charm quark pair,
- 0.59 is the charm hadronization fraction to a D^0 meson [32],
- and $\epsilon_{\text{total,sig}}$ is the signal efficiency, which is the product of the reconstruction and selection efficiency.

The total expected number of background candidates B is given by

$$B = N_Z \left(\sum_{q=c,b,s,u,d,\tau} \mathcal{B}(Z \to q\bar{q}) \epsilon_{\text{total,q}} \right), \tag{3.9}$$

where:

- $\mathcal{B}(Z \to q\bar{q})$ are the branching fractions of the Z boson to various quark final states,
- $\epsilon_{\text{total,q}}$ represents the total efficiency for each inclusive background category q, which is the product of the reconstruction and selection efficiency.

The efficiencies, after each analysis step, for all inclusive background samples as well as the signal are documented in Table 2. The most dominant contributions to the background come from $D^0 \to K_L^0 \pi^+\pi^-$ decays, making up 45.55% of the total background, and $K_S^0 \to \pi^+\pi^-$ decays. making up 16.70%.

Process	Reconstruction $[10^{-2}]$	Preselection $[10^{-3}]$	BDT1 $[10^{-2}]$	BDT2 $[10^{-4}]$	Overall
$Z \to c\bar{c}$	66.3	95.1	30.3	6.7	1.3×10^{-5}
$Z \to b\bar{b}$	84.1	2.2	4.5	2.6	2.2×10^{-8}
$Z \to u\bar{u}$	36.7	2.3	3.3	5.4	1.5×10^{-8}
$Z \to d\bar{d}$	34.8	2.4	3.4	7.5	2.1×10^{-8}
$Z \to s\bar{s}$	51.0	1.4	4.5	26.2	8.4×10^{-8}
$Z \to \tau^+\tau^-$	36.7	2.3	3.3	0.0	4.9×10^{-8}
Signal	63.4	612.6	76.9	375.6	1.1×10^{-2}

Table 2: Efficiencies at different selection steps for all inclusive background samples and signal. The selection efficiencies are calculated relative to the previous step by summing over the candidate misidentification weights w.

The significance as a function of the assumed branching fraction is illustrated in Figure 5 in comparison to the predicted upper limits from possible BSM contributions [10]. The solid orange line corresponds to the upper limits under the assumption of conservation of lepton universality, the dotted line to charged lepton flavour conservation, and the dashed line to an arbitrary flavour structure, which could result in the largest signal branching fraction at the level of $\sim 6 \times 10^{-6}$. The minimal branching fractions leading to significances of 3σ (5σ) are found to be 9.7×10^{-7} (1.6×10^{-6}), which is within the parameter space allowed in BSM models.

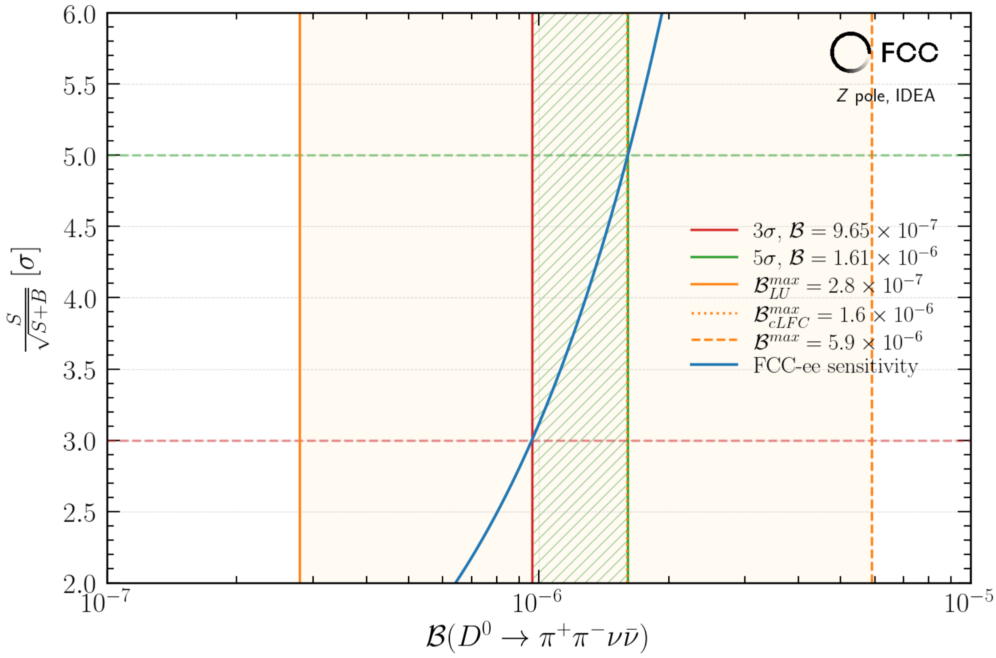

Figure 5: Sensitivity estimate as a function of the branching fraction of $D^0 \to \pi^+\pi^-\nu\bar{\nu}$(blue) with the 3σ (red) and 5σ (green) threshold. The expected theoretical maximum branching fraction for different flavour structure assumptions is marked with the orange bands.

4 Conclusion

In this note, a preliminary sensitivity study for the decay $D^0 \to \pi^+\pi^-\nu\bar{\nu}$ as a standard candle for the potential of rare charm decays with two neutrinos in the final state at FCC-ee, operated at the Z pole, is presented. While $D^0 \to \pi^+\pi^-\nu\bar{\nu}$ decays are highly suppressed and approximate null tests of the SM, BSM contributions can result in branching fractions at the level of $\mathcal{O}(10^{-6})$. This study estimates that branching fractions at the level of $\mathcal{O}(10^{-6})$ are within reach. This opens the door to a new area in flavour physics and the opportunity to look for new phenomena in processes that have not yet been explored experimentally.

Further improved studies will be done which are planned to result in a subsequent publication. A jet flavour tagger is planned to be retrained using the inclusive background sample employed in this study, incorporating a more extensive decay table than that used in the winter2023 campaign. Additional enhancements, such as K_L^0 vetoes using information of the calorimeters, a corrected mass [33] and improved machine learning techniques, are also under consideration.

The presented study is still preliminary and selection, employed variables, mechanisms and therefore results might vary in the future.

A Appendix

The variables used in the preselection and BDT trainings are shown in subsection A.1, subsection A.2 and subsection A.3. The correlations of variables used in the first and second BDT for the signal and background are shown in subsection A.4. Additionally, the separation and variable importance of the variables used in either BDT are shown in subsection A.5.

A.1 Preselection variable distributions

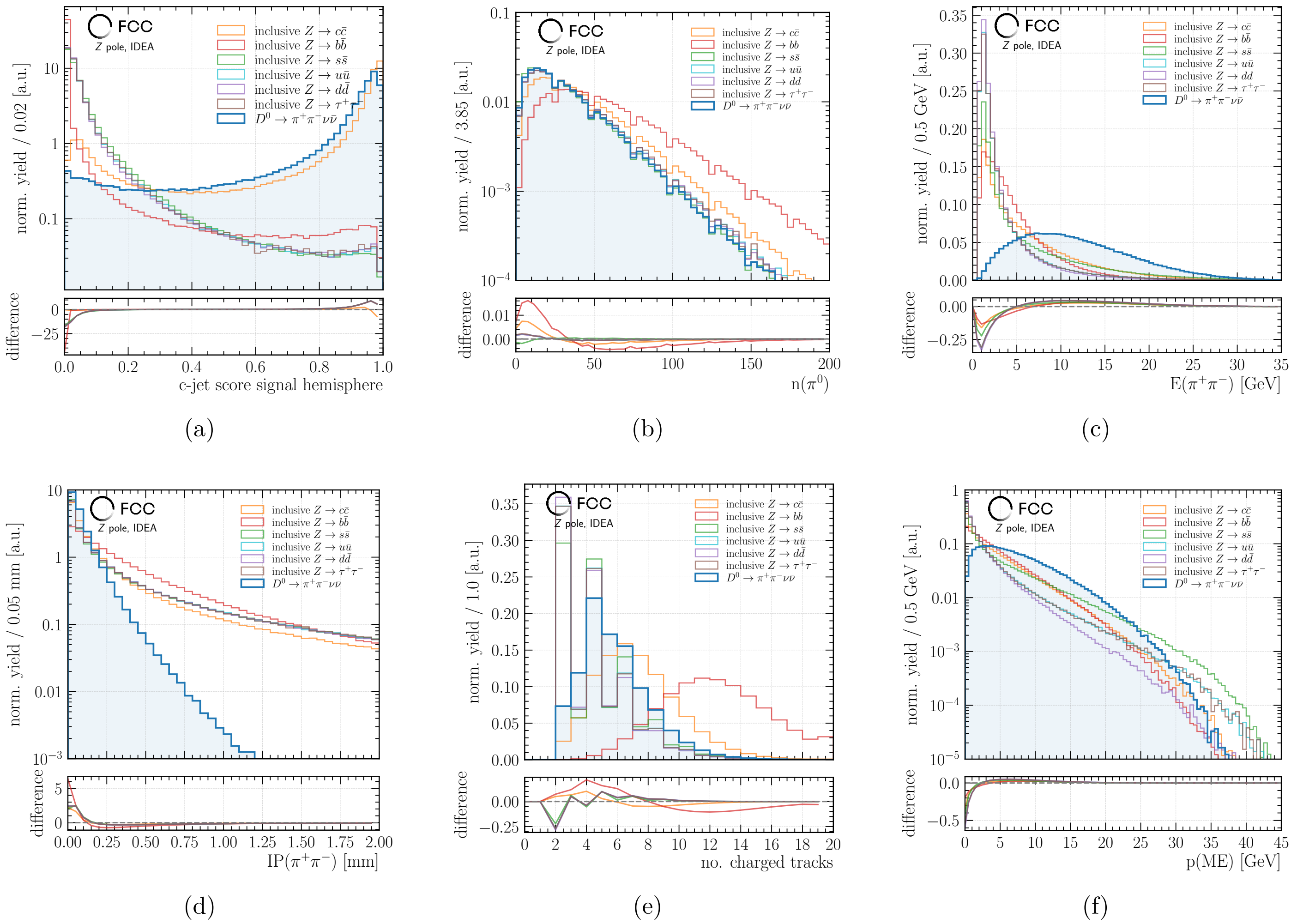

Figure 6: Variable distributions used in the preselection. (a) shows the jet flavour tagger response for the c-jet likelihood on the signal hemisphere, (b) the number of reconstructed π^0 candidates, (c) the reconstructed energy of the D^0 candidate, (d) the impact parameter of the D^0 candidate, (e) the total number of charged tracks in the event and (f) the mising energy of the event.

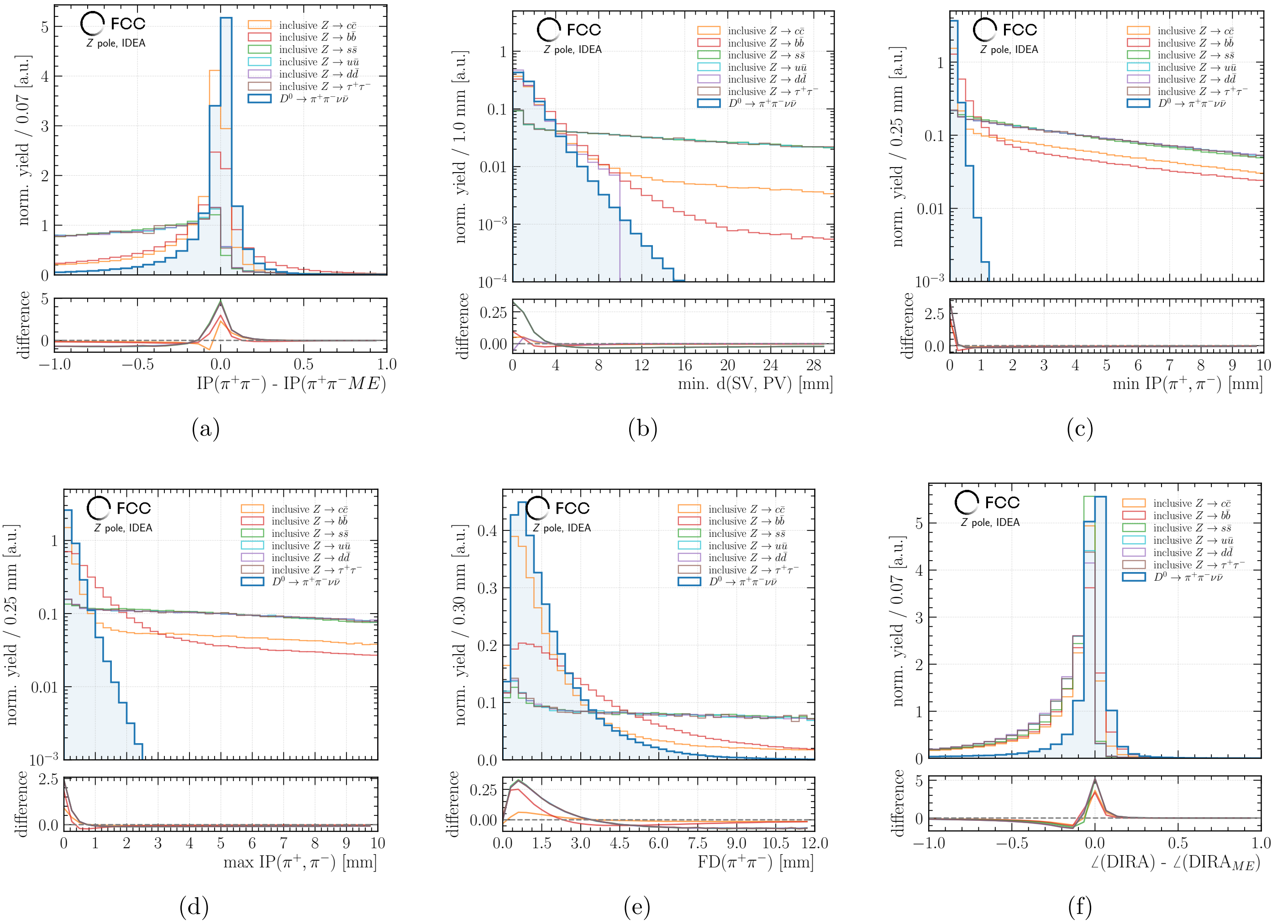

Figure 7: Variable distributions used in the preselection. (a) shows the difference of the impact parameter between reconstructed D^0 using two pions and using two pions together with the missing energy, (b) the minimum distance between all secondary vertices and the primary vertex, (c) and (d) the minimum and maximum impact parameter of either pion used for the reconstruction of the D^0 candidate, (e) the flight distance of the D^0 candidate and (f) the difference of the direction angle between reconstructed D^0 using two pions and using two pions together with the missing energy.

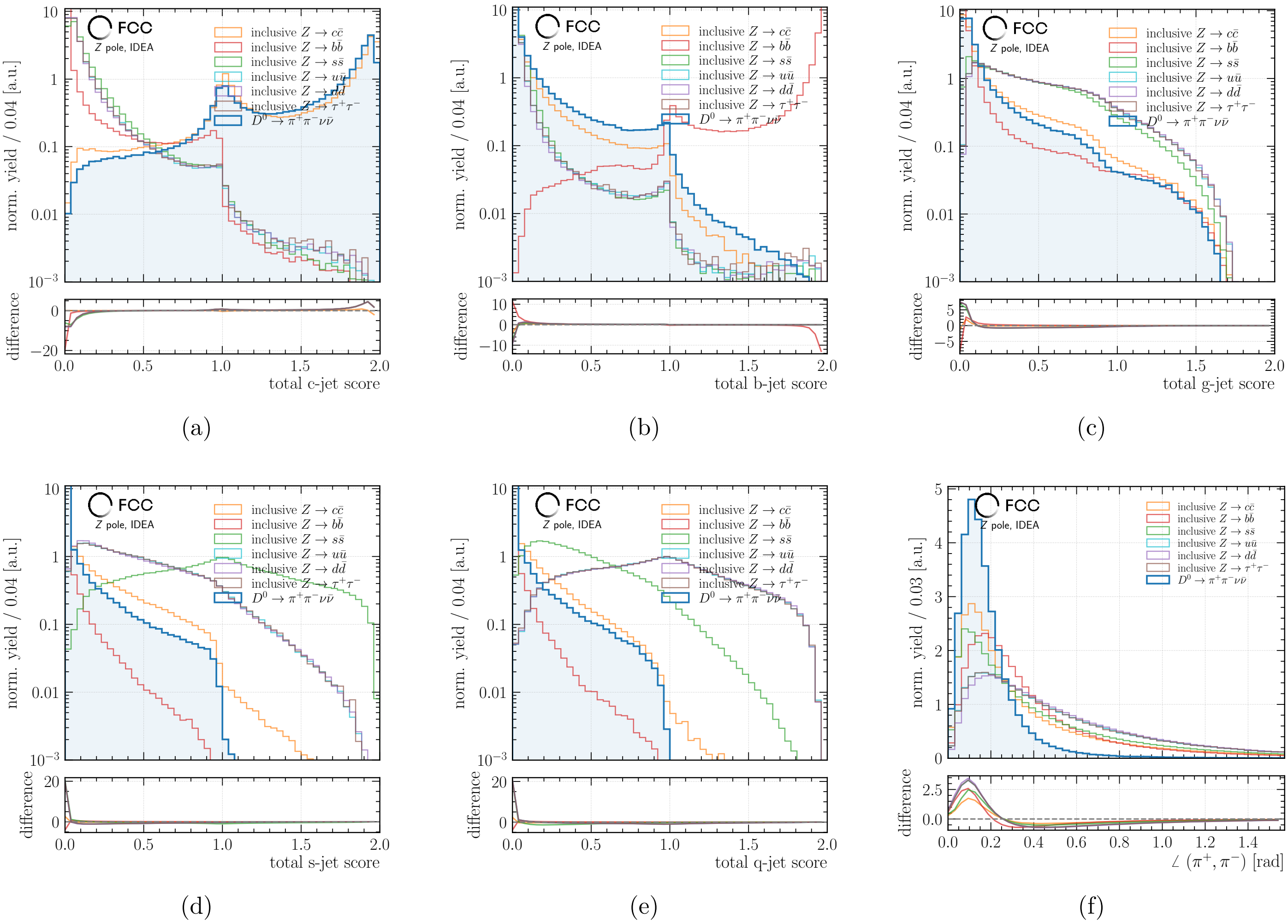

Figure 8: Variable distributions used in preselection. (a) shows the total (signal + non-signal hemisphere) jet flavour tagger response for the c-jet likelihood, (b) for b-jets, (c) for gluon jets, (d) for s-jets and (e) for u and d quarks. (f) depicts the opening angle of the two pions used for the signal reconstruction.

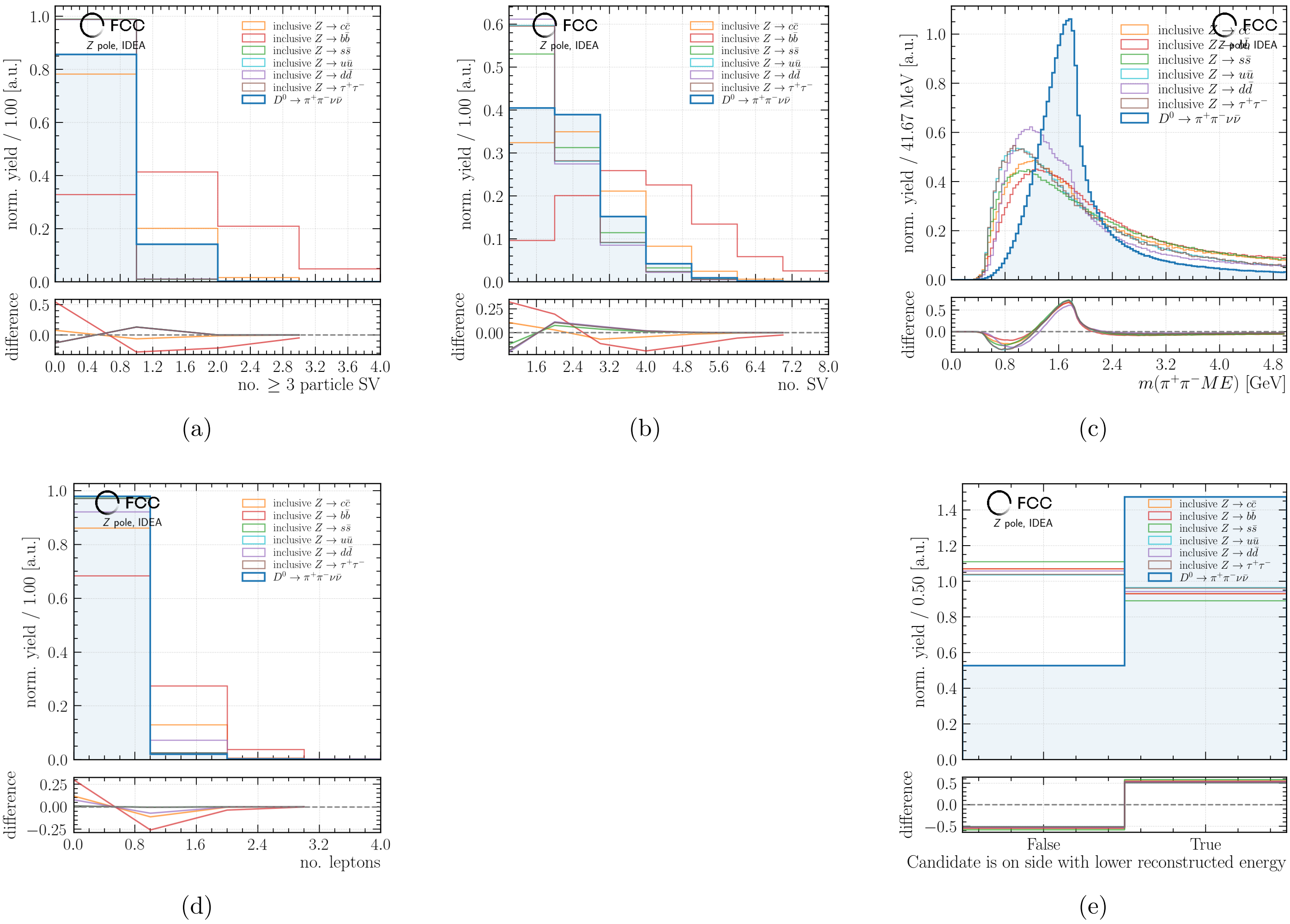

Figure 9: Variable distributions used in preselection. (a) shows the number of 3-particle secondary vertices, (b) the total number of secondary vertices, (c) the reconstructed D^0 mass using the two pions together with the missing energy, (d) the number of charged leptons in the signal hemisphere and (e) a binary distribution whether the D^0 candidate is on the hemisphere with lower reconstructed energy.

A.2 BDT1 variable distributions

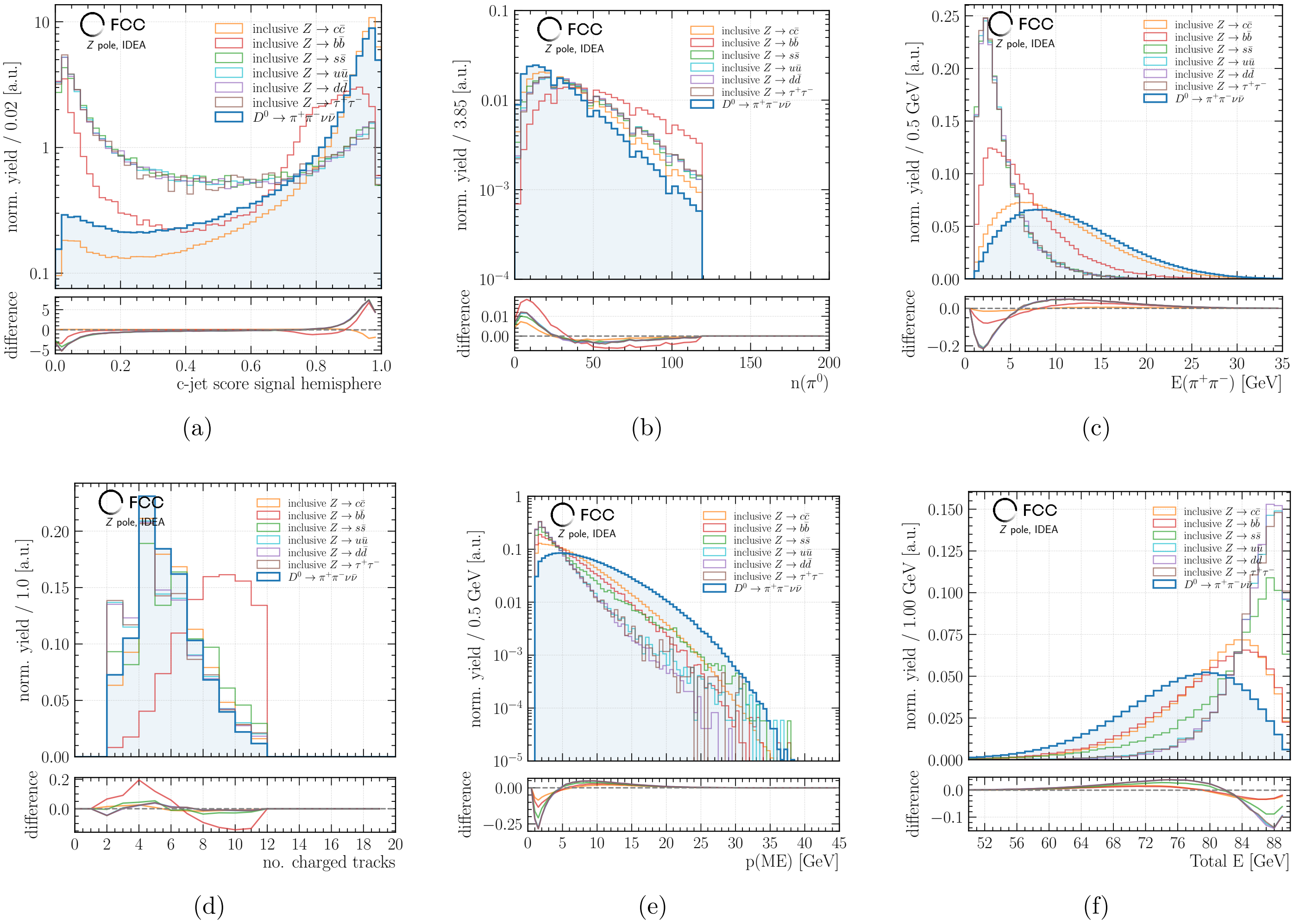

Figure 10: Variable distributions used in the BDT1. (a) shows the jet flavour tagger response for the c-jet likelihood on the signal hemisphere, (b) the number of reconstructed π^0 candidates, (c) the reconstructed energy of the D^0 candidate, (d) the the total number of charged tracks in the event, (e) the mising energy of the event and (f) the total reconstructed energy of the event.

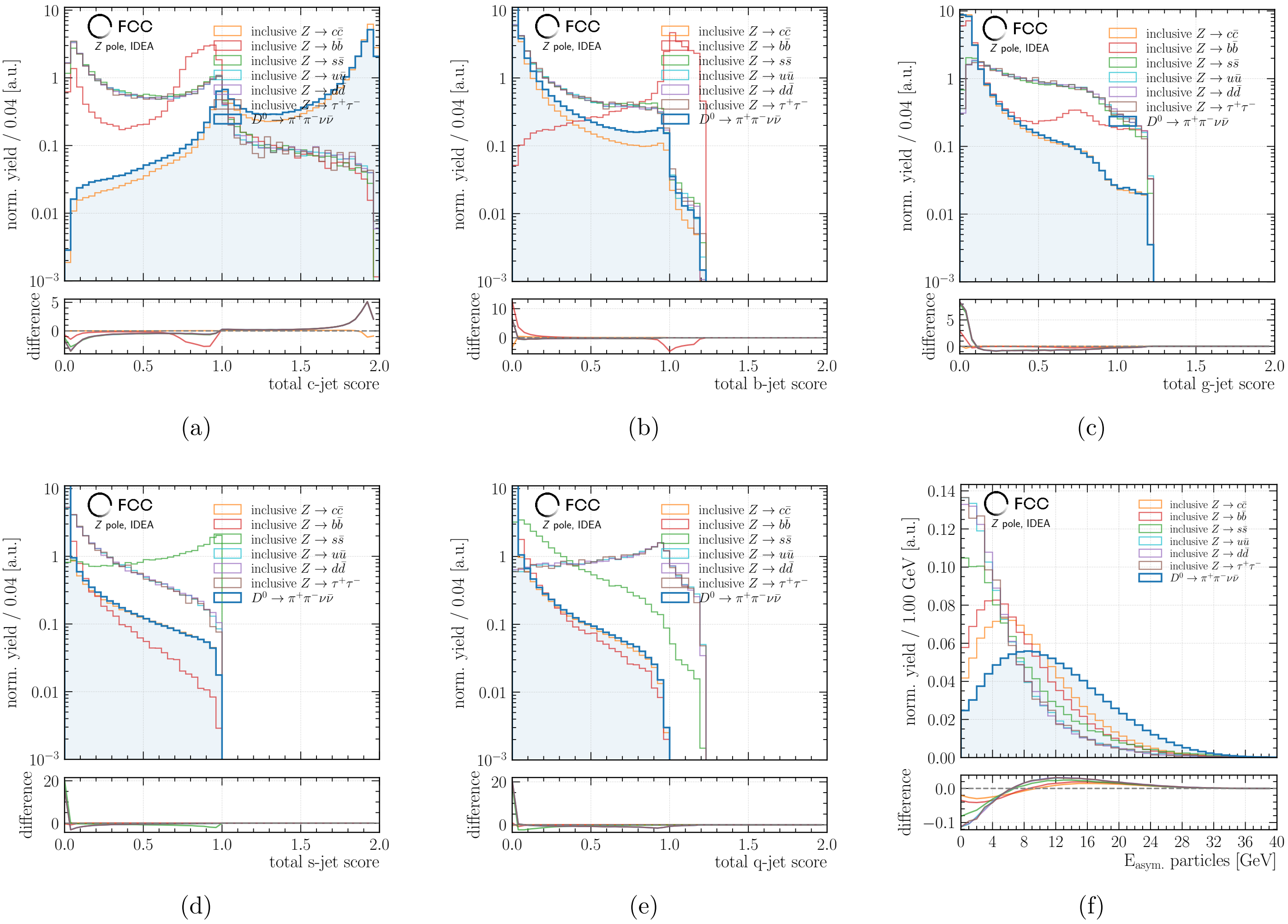

Figure 11: Variable distributions used in the BDT1. (a) shows the total (signal + non-signal hemisphere) jet flavour tagger response for the c-jet likelihood, (b) for b-jets, (c) for gluon jets, (d) for s-jets and (e) for u and d quarks. (f) depicts the energy asymmetry of particles between the signal and non-signal hemisphere.

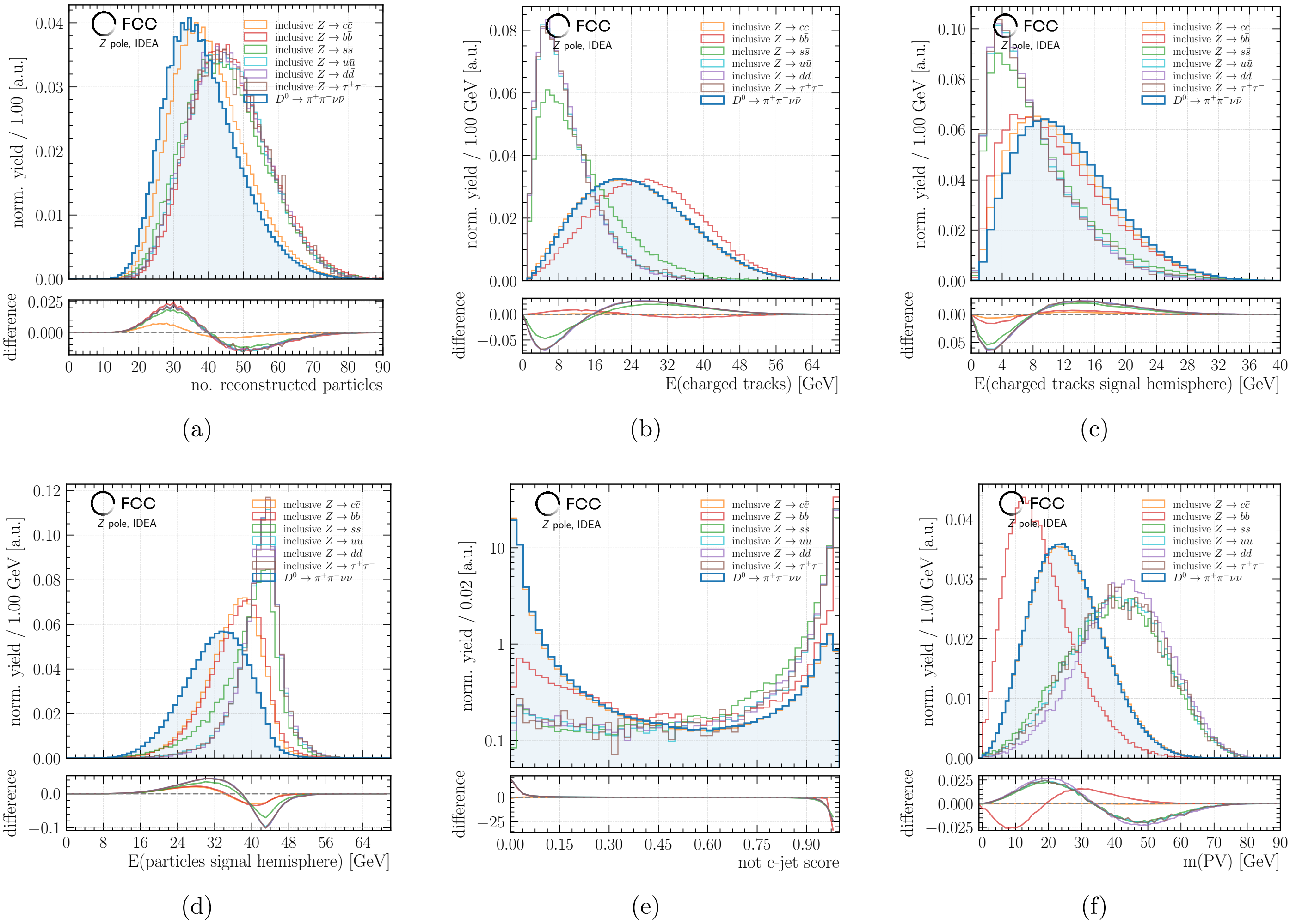

Figure 12: Variable distributions used in the BDT1. (a) shows the total number of reconstructed particles, (b)the energy of all charged track, (c) the energy of all charged tracks in the signal hemisphere, (d) the energy of all particles in the signal hemisphere, (e) the sum of the s,b,g and q-score of the jet flavour tagger on the signal hemisphere and (f) the resonstructed mass of the primary vertex using tracks classified as primary tracks.

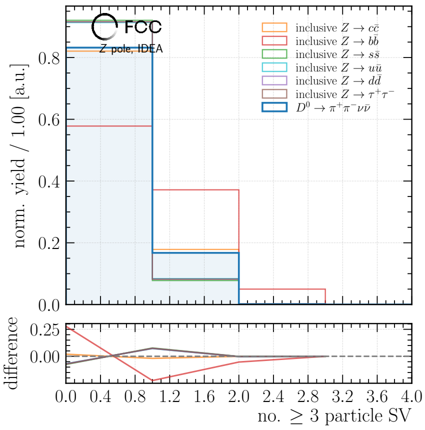

(a)

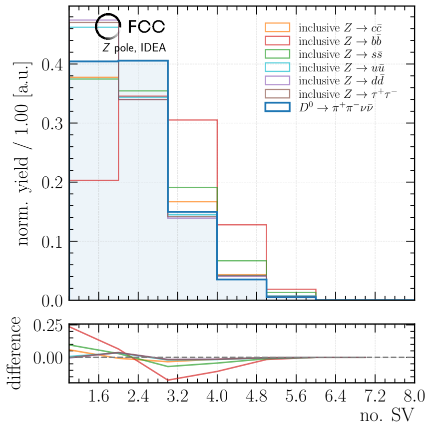

(b)

Figure 13: Variable distributions used in the BDT1. (a) shows the number of 3-particle secondary vertices and (b) the total number of secondary vertices.

A.3 BDT2 variable distributions

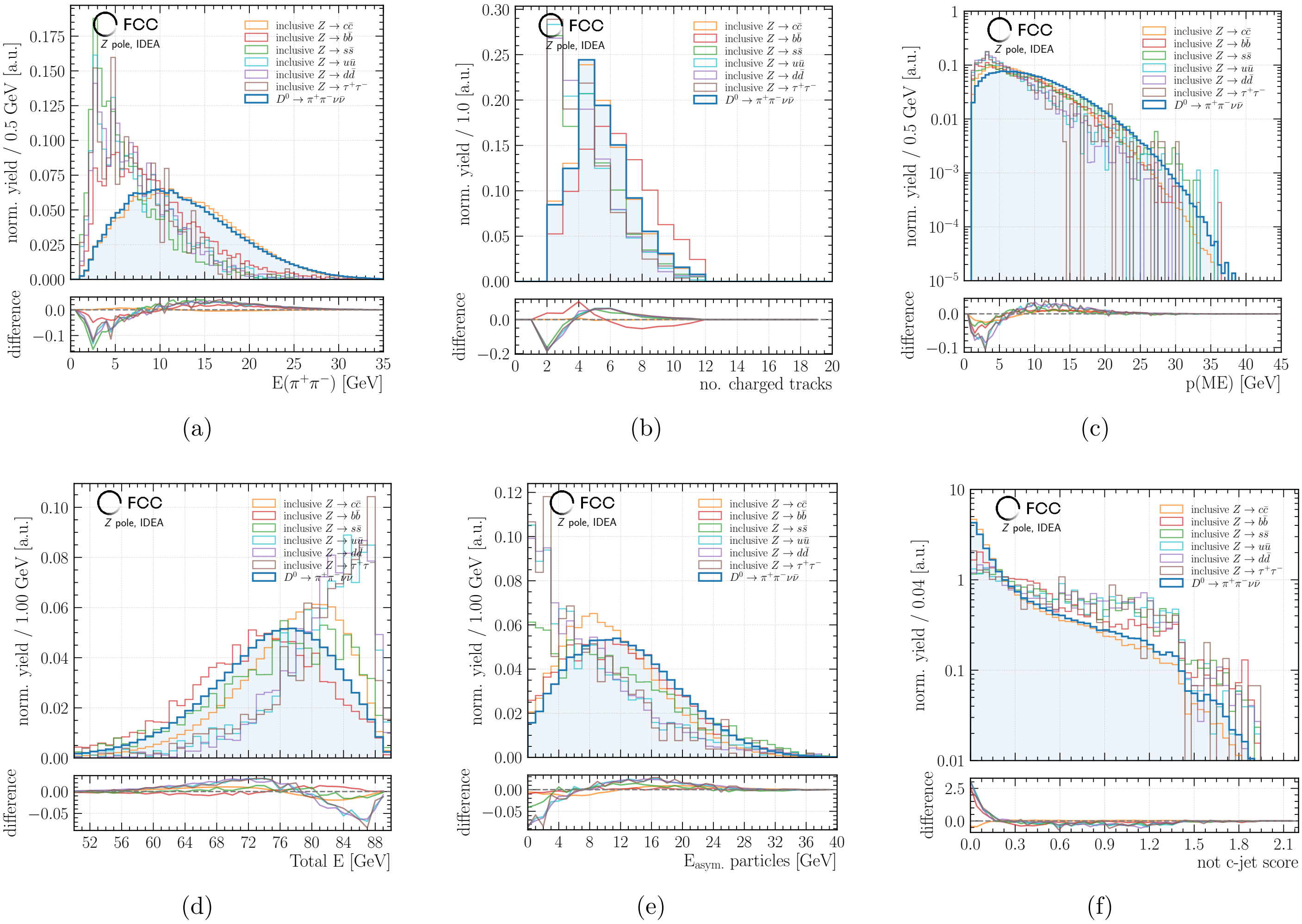

Figure 14: Variable distributions used in the BDT2. (a) shows the reconstructed energy of the D^0 candidate, (b) the total number of charged tracks in the event, (c) the mising energy of the event, (d) the total reconstructed energy of the event, (e) the energy asymmetry of particles between the signal and non-signal hemisphere and (f) the sum of the s,b,g and q-score of the jet flavour tagger on both hemispheres substracted by the c-jet flavour tagger score on the signal hemisphere.

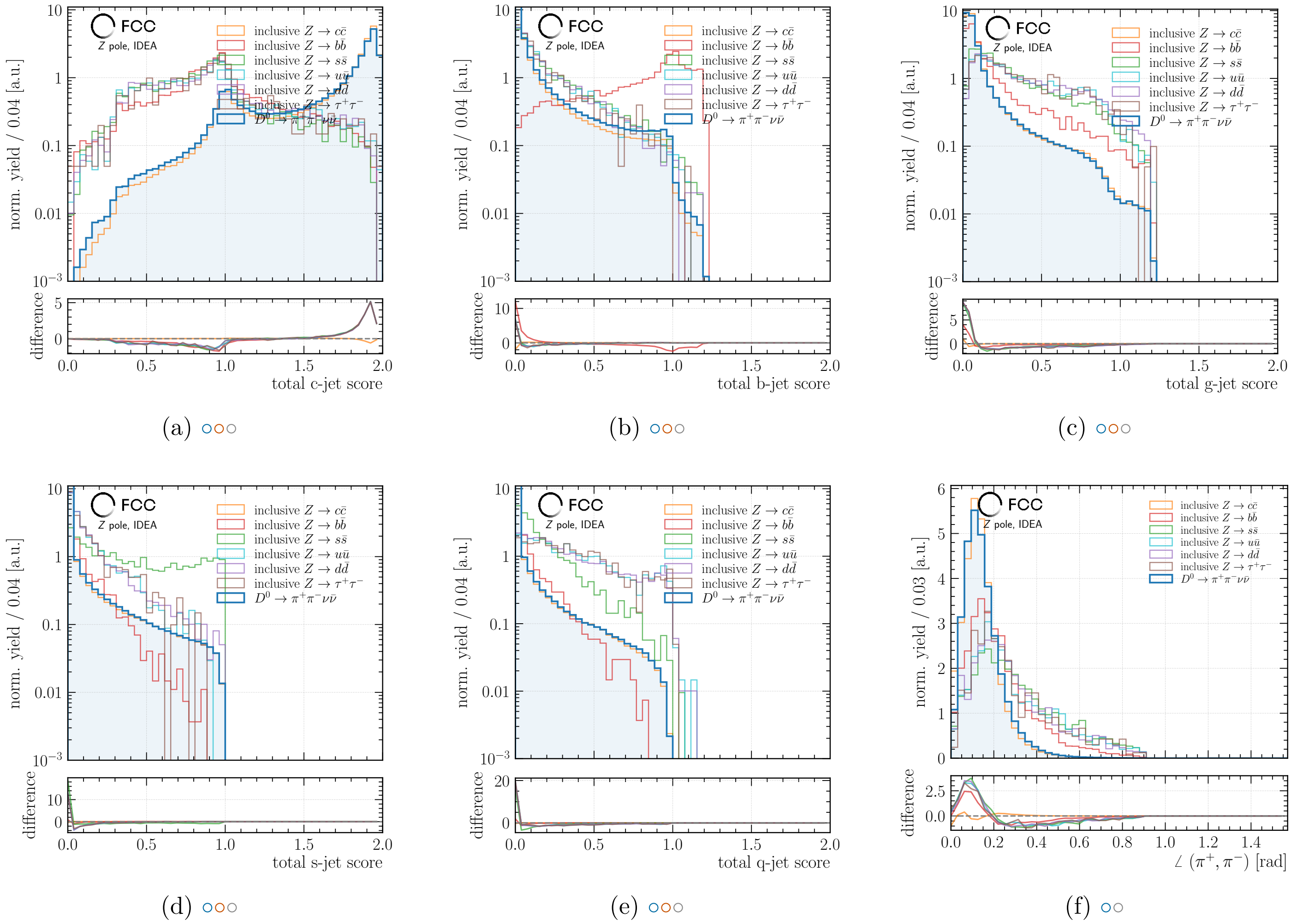

Figure 15: Variable distributions used in the BDT2. (a) shows the total (signal + non-signal hemisphere) jet flavour tagger response for the c-jet likelihood, (b) for b-jets, (c) for gluon jets, (d) for s-jets and (e) for u and d quarks. (f) depicts the opening angle of the two pions used for the signal reconstruction.

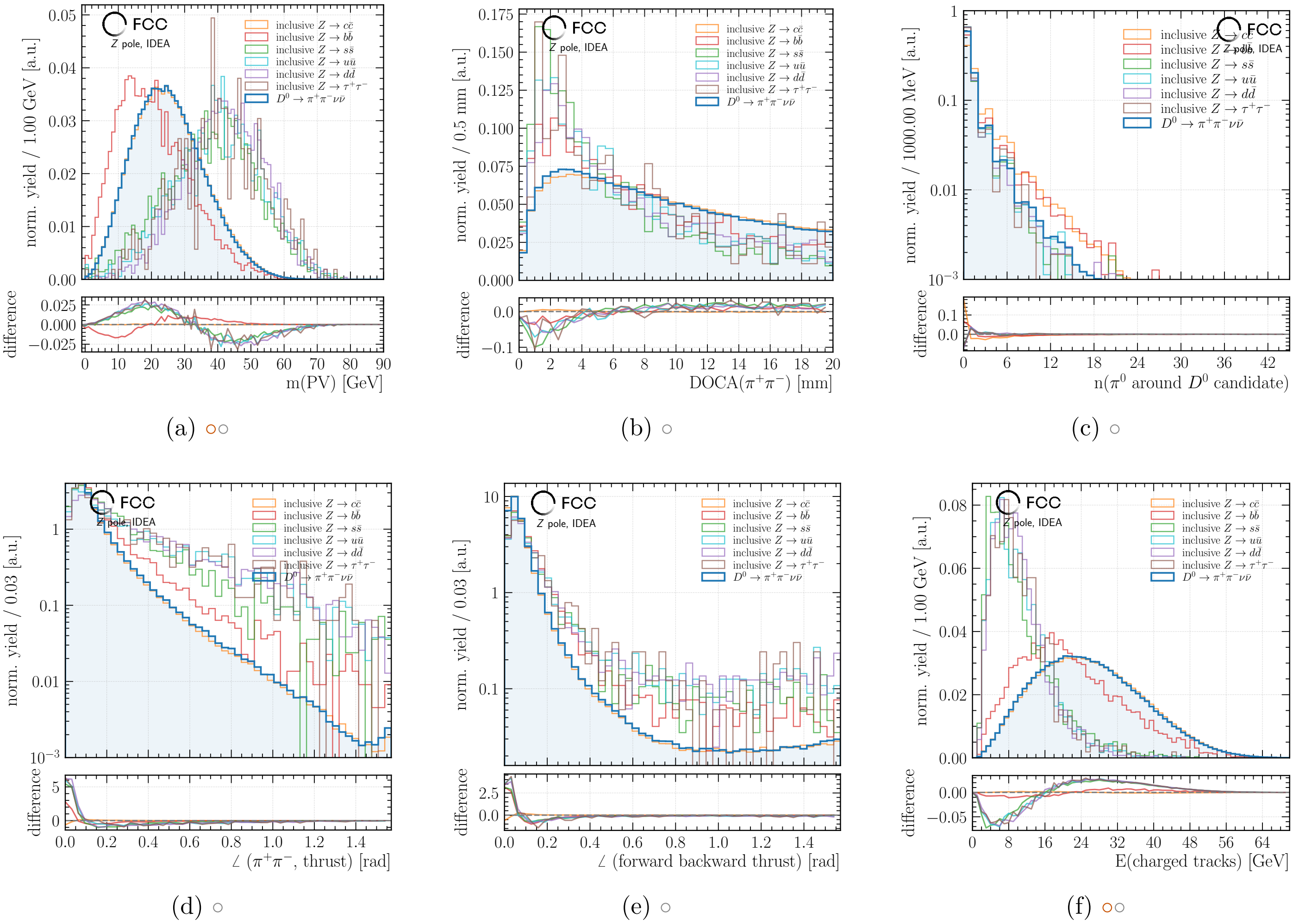

Figure 16: Variable distributions used in the BDT2. (a) shows the reconstructed mass of the primary vertex using tracks classified as primary tracks, (b) he closest approach of the pion tracks used for the D^0 reconstruction, (c) the number of π^0 candidates within a defined angular distance around the D^0 candidate, (d) the angle between the reconstructed D^0 momentum and the thrust axis, (e) the angle between the thrusts calculated for either hemisphere and (f) the energy of all charged tracks.

A.4 Correlation plots

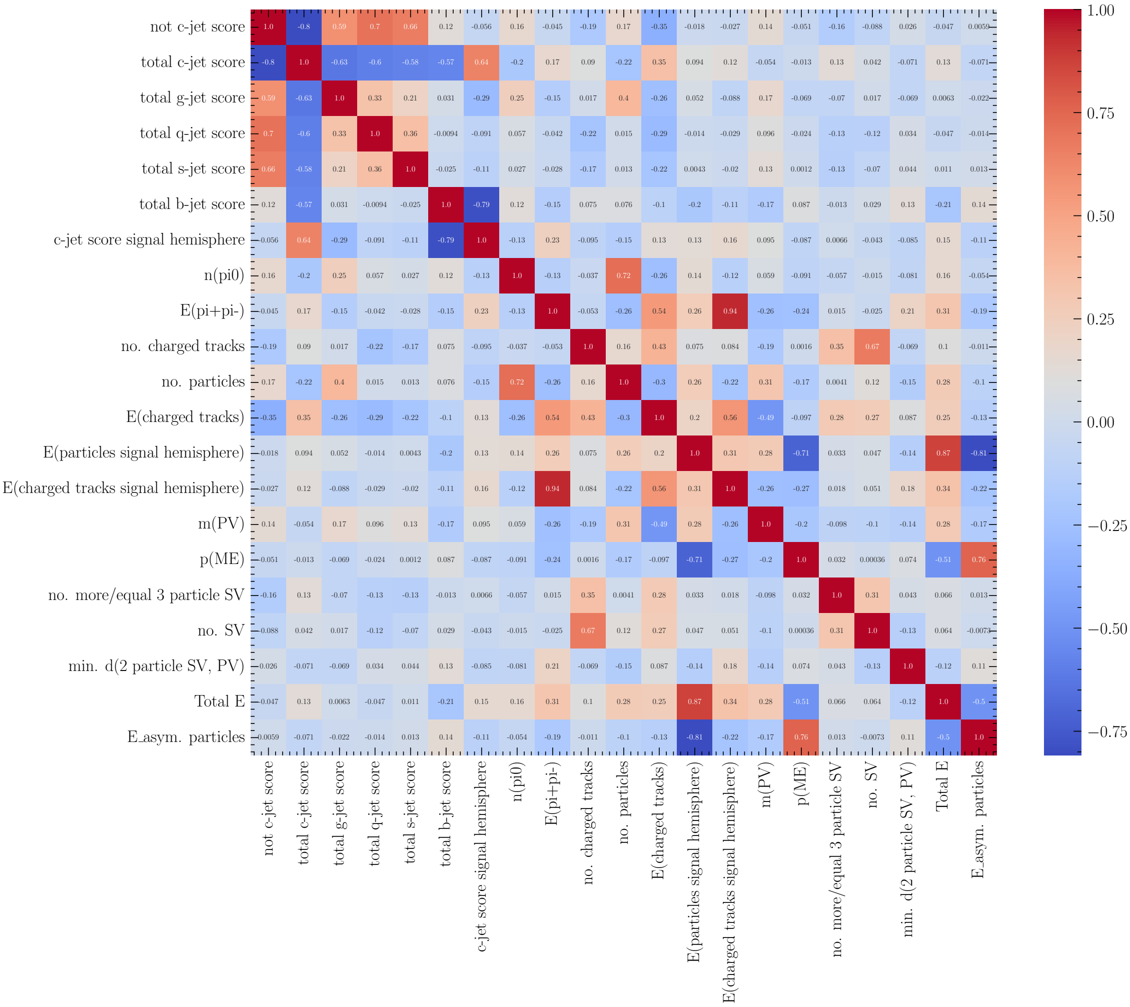

Figure 17: Correlation of variables used in the training of the first BDT for the signal.

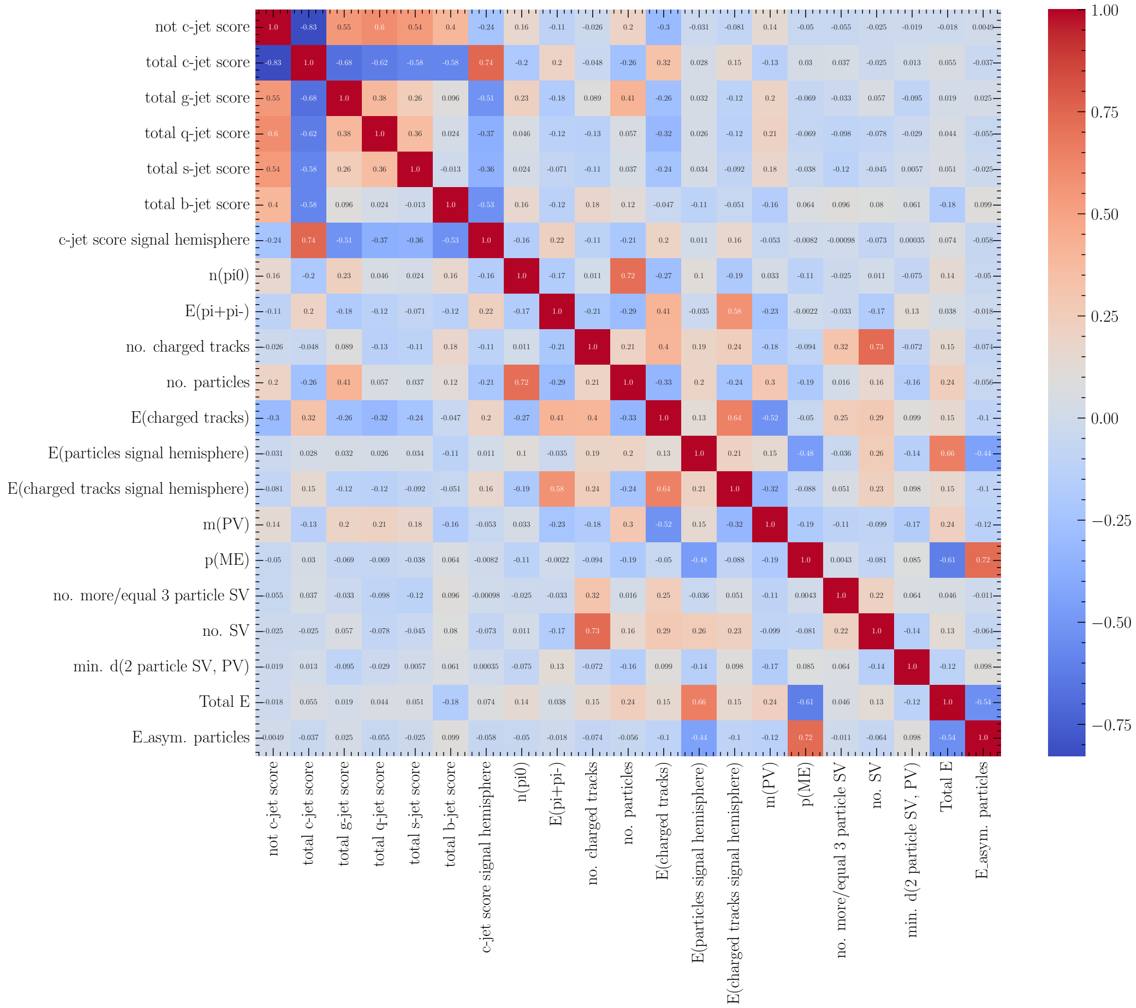

Figure 18: Correlation of variables used in the training of the first BDT for the background.

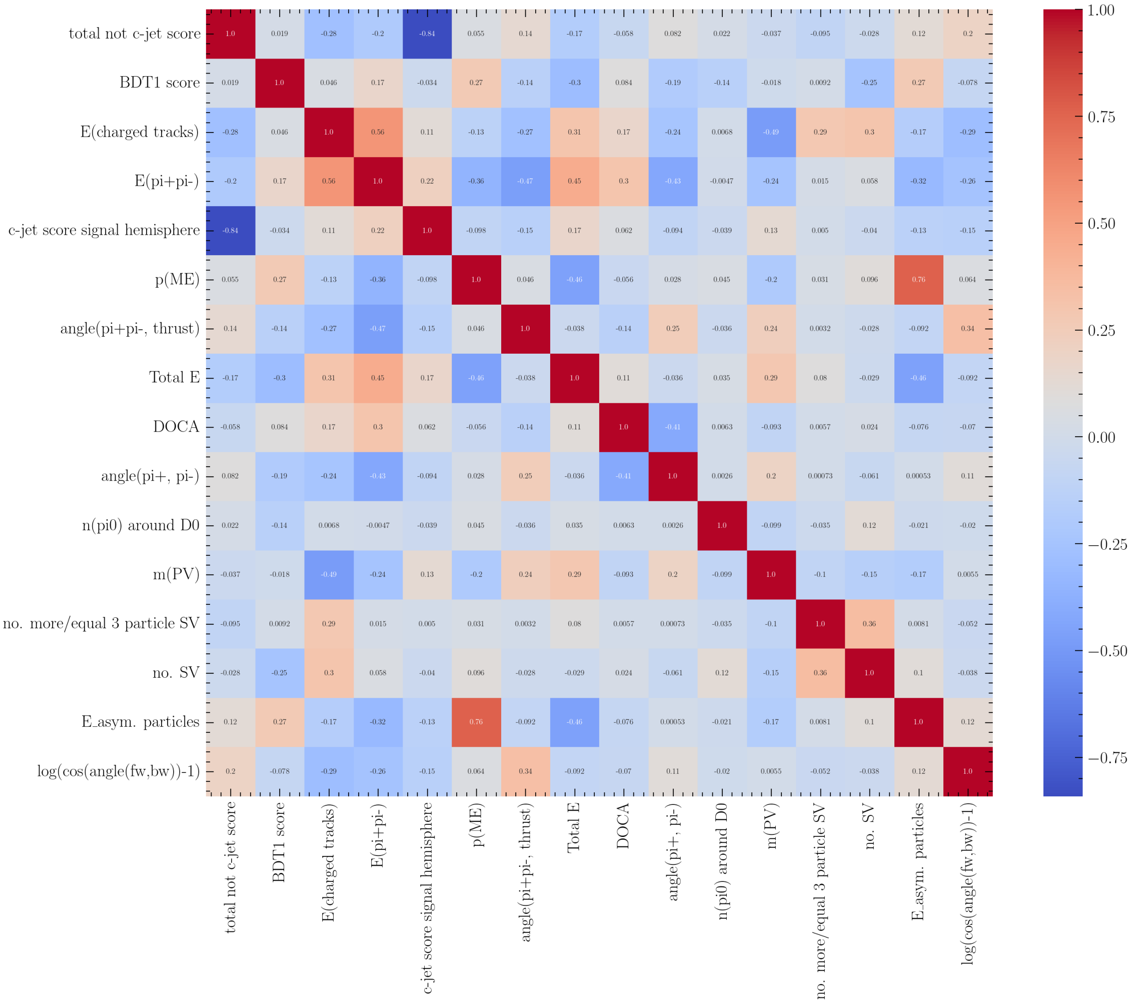

Figure 19: Correlation of variables used in the training of the second BDT for the signal.

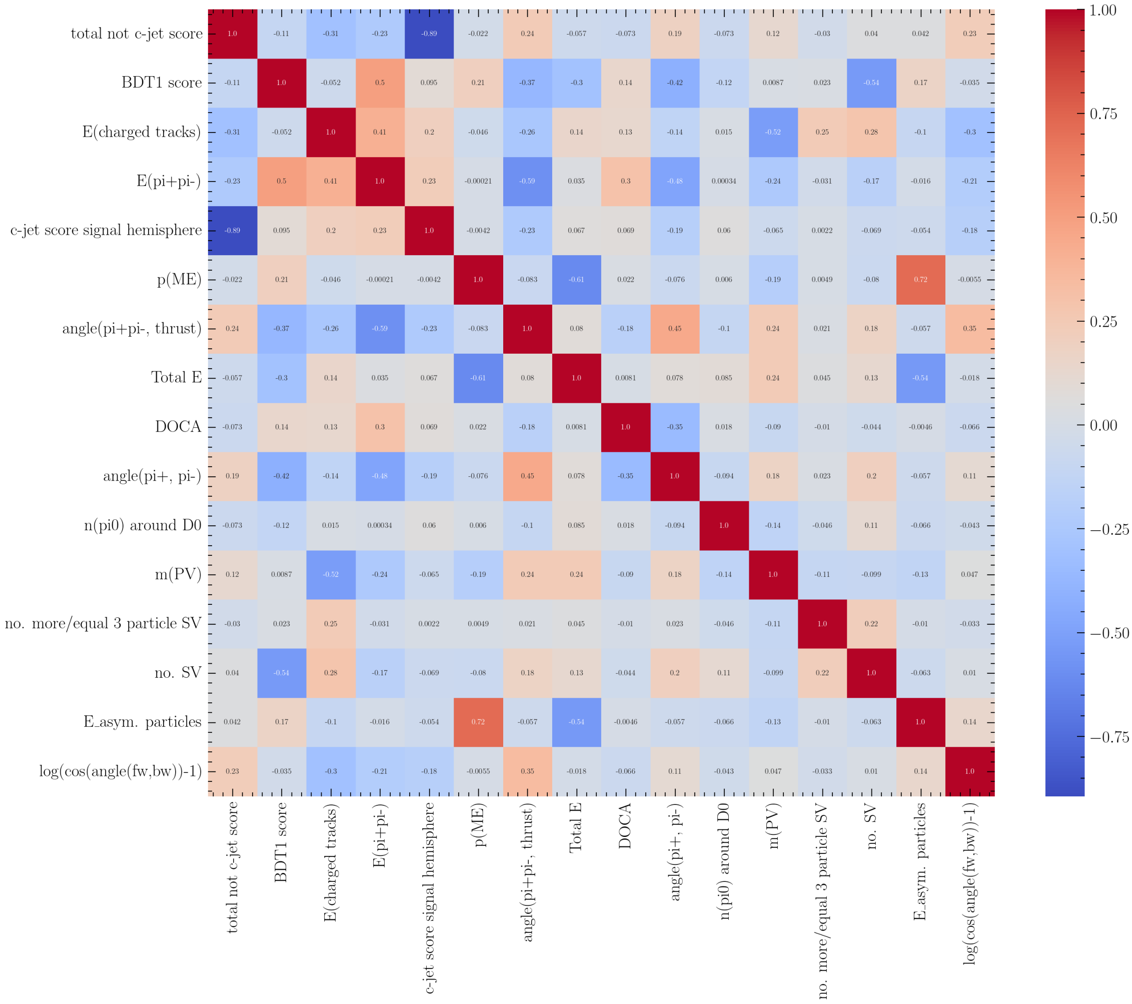

Figure 20: Correlation of variables used in the training of the second BDT for the background.

A.5 Separation and Variable Importance

Variable	Separation	Variable Importance
E(particles signal hemisphere)	1.872×10^{-1}	1.269×10^{-1}
$E(\pi^+\pi^-)$	1.297×10^{-1}	1.015×10^{-1}
Total E	9.752×10^{-2}	7.141×10^{-2}
p(ME)	7.076×10^{-2}	3.751×10^{-2}
no. SV	5.561×10^{-2}	3.648×10^{-2}
$E_{\text{asym.}}$ particles	5.140×10^{-2}	3.755×10^{-2}
c-jet score signal hemisphere	4.159×10^{-2}	6.929×10^{-2}
total c-jet score	3.987×10^{-2}	5.898×10^{-2}
no. charged tracks	3.856×10^{-2}	1.736×10^{-2}
not c-jet score	2.826×10^{-2}	5.035×10^{-2}
no. particles	2.703×10^{-2}	4.148×10^{-2}
$n(\pi^0)$	2.337×10^{-2}	2.579×10^{-2}
total q-jet score	2.137×10^{-2}	3.582×10^{-2}
E (charged tracks signal hemisphere)	1.770×10^{-2}	8.151×10^{-2}
total s-jet score	1.487×10^{-2}	2.143×10^{-2}
total g-jet score	1.486×10^{-2}	3.124×10^{-2}
total b-jet score	1.412×10^{-2}	5.070×10^{-2}
E (charged tracks)	8.464×10^{-3}	2.193×10^{-2}
m(PV)	7.482×10^{-3}	2.510×10^{-2}
min. d(2 particle SV, PV)	1.806×10^{-3}	4.009×10^{-2}
no. ≥ 3 particles SV	8.841×10^{-4}	1.761×10^{-2}

Table 3: BDT1 variables and their corresponding separational power and variable importance, sorted descending by the separation.

Variable	Separation	Variable Importance
BDT1 score	3.927×10^{-2}	8.195×10^{-2}
$n(\pi^0)$ around D^0	3.901×10^{-2}	9.090×10^{-2}
Total E	2.766×10^{-2}	6.538×10^{-2}
p(ME)	2.002×10^{-2}	4.083×10^{-2}
$E_{\text{asym.}}$ particles	1.815×10^{-2}	2.970×10^{-2}
$\angle(\pi^+\pi^-)$	6.269×10^{-3}	1.905×10^{-1}
total b-jet score	4.455×10^{-3}	4.598×10^{-2}
c-jet score signal hemisphere	3.223×10^{-3}	2.715×10^{-2}
total not c-jet score	1.947×10^{-3}	1.486×10^{-2}
total c-jet score	1.472×10^{-3}	2.747×10^{-2}
$E(\pi^+\pi^-)$	1.370×10^{-3}	1.596×10^{-1}
no. SV	1.320×10^{-3}	4.650×10^{-2}
$\angle(\pi^+\pi^-, \text{thrust})$	4.520×10^{-4}	2.890×10^{-2}
$\angle(\text{fw}, \text{bw})$	4.017×10^{-4}	2.155×10^{-2}
m(PV)	2.639×10^{-4}	2.383×10^{-2}
DOCA	2.630×10^{-4}	2.056×10^{-2}
total s-jet score	1.590×10^{-4}	2.871×10^{-2}
E (charged tracks)	1.443×10^{-4}	1.940×10^{-2}
no. ≥ 3 particles SV	1.175×10^{-4}	1.569×10^{-2}
total q-jet score	1.117×10^{-4}	2.055×10^{-2}

Table 4: BDT2 variables and their corresponding separational power and variable importance, sorted descending by the separation.

References

[1] ATLAS Collaboration. Observation of a new particle in the search for the standard model higgs boson with the atlas detector at the lhc. *Physics Letters B*, 716(1):1–29, 2012.

[2] CMS Collaboration. Observation of a new boson at a mass of 125 GeV with the CMS experiment at the LHC. *Physics Letters B*, 716(1):30–61, 2012.

[3] A. Abada, M. Abbrescia, S. S. Abdus Salam, I. Abdyukhanov, J. Abelleira Fernandez, A. Abramov, M. Aburaia, A. O. Acar, P. R. Adzic, P. Agrawal, and J. A. Aguilar-Saavedra. FCC-ee: The Lepton Collider. *The European Physical Journal Special Topics*, 228(2):261–623, 06 2019.

[4] Yasmine Amhis, Matthew Kenzie, Méril Reboud, and Aidan R. Wiederhold. Prospects for searches of $b \to s\nu\bar{\nu}$ decays at FCC-ee. *Journal of High Energy Physics*, 2024(1):144, 2024.

[5] Xunwu Zuo, Marco Fedele, Clément Helsens, Donal Hill, Syuhei Iguro, and Markus Klute. Prospects for B_c^+ and $B^+ \to \tau^+\nu_\tau$ at FCC-ee. *The European Physical Journal C*, 84(1):87, 2024.

[6] Tristan Miralles and Stéphane Monteil. Study of the feasibility of the observation of $B^0 \to K^*(892)\tau^+\tau^-$ at FCC-*ee* and related vertex detector performance requirements, September 2024.

[7] LHCb Collaboration. The LHCb Physics Programme. In *34th Rencontres de Moriond: QCD and Hadronic interactions*, pages 409–414, Hanoi, 2001. The Gioi.

[8] Belle II Collaboration. The belle ii physics book. *Progress of Theoretical and Experimental Physics*, 2019(12):123C01, 12 2019.

[9] Hector Gisbert, Marcel Golz, and Dominik Stefan Mitzel. Theoretical and experimental status of rare charm decays. *Mod. Phys. Lett.*, A36(04):2130002, 2021.

[10] Rigo Bause, Hector Gisbert, Marcel Golz, and Gudrun Hiller. Rare charm $\boldsymbol{c \to u\,\nu\bar{\nu}}$ dineutrino null tests for e^+e^- machines. *Phys. Rev. D*, 103(1):015033, 2021.

[11] Marcel Golz, Gudrun Hiller, and Tom Magorsch. Probing for new physics with rare charm baryon $(\Lambda_c, \Xi_c\Omega_c)$ decays. *JHEP*, 09:208, 2021.

[12] Rigo Bause, Hector Gisbert, Marcel Golz, and Gudrun Hiller. Lepton universality and lepton flavor conservation tests with dineutrino modes. *Eur. Phys. J. C*, 82(2):164, 2022.

[13] M. Antonello. IDEA: A detector concept for future leptonic colliders. *Nuovo Cim. C*, 43(2-3):27, 2020.

[14] Gabriella Gaudio. The IDEA detector concept for FCCee. *PoS*, ICHEP2022:337, 11 2022.

[15] Torbjörn Sjöstrand, Stefan Ask, Jesper R. Christiansen, Richard Corke, Nishita Desai, Philip Ilten, Stephen Mrenna, Stefan Prestel, Christine O. Rasmussen, and Peter Z. Skands. An introduction to pythia 8.2. *Computer Physics Communications*, 191:159–177, 2015.

[16] FCC Collaboration. `https://hep-fcc.github.io/FCCeePhysicsPerformance/General/#common-event-samples`. Accessed: 2025-02-18.

[17] David J. Lange. The evtgen particle decay simulation package. *Nuclear Instruments and Methods in Physics Research Section A: Accelerators, Spectrometers, Detectors and Associated Equipment*, 462(1):152–155, 2001. BEAUTY2000, Proceedings of the 7th Int. Conf. on B-Physics at Hadron Machines.

[18] Belle II Collaboration. `https://github.com/belle2/basf2/blob/main/decfiles/dec/DECAY_BELLE2.DEC`. Accessed: 2025-02-18.

[19] The DELPHES 3 Collaboration. Delphes 3: a modular framework for fast simulation of a generic collider experiment. *Journal of High Energy Physics*, 2014(2):57, 02 2014.

[20] J. de Favereau, C. Delaere, P. Demin, A. Giammanco, V. Lemaître, A. Mertens, and M. Selvaggi. Delphes 3: A modular framework for fast simulation of a generic collider experiment, 2014. https://github.com/delphes/delphes.

[21] F. et al. Bedeschi. Idea: A detector concept for future leptonic colliders. *Il Nuovo Cimento C*, 43(2):27, 2020.

[22] Guy Wilkinson. Particle identification at FCC-ee. *Eur. Phys. J. Plus*, 136(8):835, 2021.

[23] Frank Gaede, Thomas Madlener, Placido Declara Fernandez, Gerardo Ganis, Benedikt Hegner, Clement Helsens, Andre Sailer, Graeme A. Stewart, and Valentin Voelkl. EDM4hep - a common event data model for HEP experiments. *PoS*, ICHEP2022:1237, 11 2022.

[24] Rene Brun and Fons Rademakers. Root — an object oriented data analysis framework. *Nuclear Instruments and Methods in Physics Research Section A: Accelerators, Spectrometers, Detectors and Associated Equipment*, 389(1):81–86, 1997.

[25] FCC Collaboration. `https://github.com/HEP-FCC/FCCAnalyses/blob/master/analyzers/dataframe/src/VertexFitterSimple.cc`. Accessed: 2025-01-11.

[26] Franco Bedeschi. `https://cp3.irmp.ucl.ac.be/projects/delphes/browser/git/external/TrackCovariance/VertexFit.cc?rev=7fbde86ce8d4974a568d205581184ef01d4e19c3`. Accessed: 2025-02-13.

[27] M. Hatlo, L. Moneta, F. James, and V. Innocente. Developments of the MINUIT minimization package within ROOT. 2005.

[28] Franco Bedeschi, Loukas Gouskos, and Michele Selvaggi. Jet flavour tagging for future colliders with fast simulation. *The European Physical Journal C*, 82(7), July 2022.

[29] Yoav Freund and Robert E Schapire. A decision-theoretic generalization of on-line learning and an application to boosting. *Journal of Computer and System Sciences*, 55(1):119–139, 1997.

[30] S. Navas and others (Particle Data Group). Review of particle physics. *Phys. Rev. D*, 110:030001, 2024.

[31] Giovanni Punzi. Sensitivity of searches for new signals and its optimization. In *Statistical Problems in Particle Physics, Astrophysics, and Cosmology (PHYSTAT 2003)*, 2003.

[32] Mykhailo Lisovyi, Andrii Verbytskyi, and Oleksandr Zenaiev. Combined analysis of charm-quark fragmentation-fraction measurements. *The European Physical Journal C*, 76(7), July 2016.

[33] Lucia Grillo. New physics searches with angular analyses of b-hadron decays. `https://cds.cern.ch/record/2911242/files/Vienna_Angular_v1.pdf`. See M_{corr} Slide 4. Accessed: 2025-03-07.